

# DNF - Galaxy photometric redshift by Directional Neighbourhood Fitting

J. De Vicente, E. Sánchez and I. Sevilla-Noarbe\*,  
*Centro de Investigaciones Energéticas, Medioambientales y Tecnológicas (CIEMAT),  
 Avda. Complutense 40, E-28040, Madrid, Spain*

11 May 2016

## ABSTRACT

Wide field images taken in several photometric bands allow simultaneous measurement of redshifts for thousands of galaxies. A variety of algorithms to make this measurement have appeared in the last few years, the majority of which can be classified as either template or training based methods. Among the latter, nearest neighbour estimators stand out as one of the most successful, in terms of both precision and the quality of error estimation. In this paper we describe the Directional Neighbourhood Fitting (DNF) algorithm based on the following: a new neighbourhood metric (Directional Neighbourhood), a photo-z estimation strategy (Neighbourhood Fitting) and a method for generating the photo-z probability distribution function. We compare DNF with other well-known empirical photometric redshift tools using different public datasets (Sloan Digital Sky Survey, VIMOS VLT Deep Survey and Photo-z Accuracy Testing). DNF achieves high-quality results with reliable error.

**Key words:** methods: data analysis – surveys – galaxies: distance and redshift – galaxies: statistics – cosmology: large-scale structure of Universe.

## 1 INTRODUCTION

Current cosmological surveys require that the redshifts of a large number of galaxies be measured to test and validate different cosmological models. Spectroscopy provides high resolution redshift measurement, at the cost of long exposure times using large telescopes. Conversely, photometric redshift estimation (photo-z) is a powerful alternative in which individual precision is relaxed in favour of statistics. In this case, a large number of low resolution galaxy redshifts are obtained from imaging in different bands. Several current and future surveys are based on the measurement of massive amounts of objects and rely on photometric redshifts to accomplish their goals in the field of cosmology, e.g., Dark Energy Survey (DES; Flaugher et al. (2005)) and Large Synoptic Survey Telescope (LSST; Ivezić et al. (2013)).

There are two basic approaches to photometric redshifts: template-based methods and training-based methods. Template based methods rely on a set of rest-frame spectra that are redshifted to fit the galaxy photometric magnitudes (Arnouts et al. (1999), Benítez (2000), Bolzonella et al. (2000), Feldmann et al. (2006)).

On the other hand, training based methods (Connolly

et al. (1995), Collister & Lahav (2004), Gerdes et al. (2010), Carrasco & Brunner (2013), Hoyle et al. (2015), Rau et al. (2015)) require a training sample, i.e. a set of imaged galaxies whose spectroscopic redshifts are known. Based on such a training sample, these methods are able to predict the photometric redshifts for a larger galaxy sample without spectroscopic measurements. A recent review of the field of photometric redshifts can be found in Zheng & Zhang (2012) and a comparison among different methods in Photo-z Accuracy Testing (PHAT; Hildebrandt et al. (2010)) and DES (Sanchez et al. (2014)).

The k-nearest neighbour (kNN) algorithm (Altman (1992)) is one of the best-known training-based approaches. For instance, Csabai et al. (2003) describe the application of this technique to the Sloan Digital Sky Survey (SDSS) Early Data Release. The authors use local interpolation in regions of colour space to reduce the photo-z dispersion. In Csabai et al. (2007), the authors instead use a kd-tree search method to efficiently find the nearest neighbours, followed by polynomial fitting. Ball et al. (2008) apply kNN to generate full photometric redshift probability density functions (PDFs) for objects in SDSS Data Release 5, obtaining results consistent with other machine learning techniques. In another study, Wang et al. (2010) compared two closely related methods, the kernel regression and the nearest neighbours algorithms, for photometric redshift estimation of

\* E-mail:juan.vicente@ciemat.es, eusebio.sanchez@ciemat.es, ignacio.sevilla@ciemat.es

quasar samples. Here, kernel regression delivered more accurate predictions, whereas kNN showed its superiority for high redshift quasars. Zhang et al. (2013) also estimate the photometric redshifts of quasars to study the influence of  $k$  value and different input patterns on performance, while Oyaizu et al. (2008) use the Nearest Neighbour algorithm to estimate the photo- $z$  error (nearest neighbour error) of other photo- $z$  techniques such as neural networks.

Another goal of photo- $z$  algorithms is to estimate the underlying redshift distribution  $N(z)$  of galaxy samples. In Lima et al. (2008), a nearest neighbour approximation is used to estimate  $N(z)$ . The method does not rely on photometric redshift estimates for individual galaxies, which typically suffer from biases. Instead, it assigns weights to galaxies in a spectroscopic subsample such that the weighted distributions of photometric observables match the corresponding distributions of the photometric sample. The weights are estimated using a nearest neighbour technique. The authors found that ‘the weighting method accurately recovers the underlying redshift distribution, typically better than the photo- $z$  reconstruction, provided that the spectroscopic subsample spans the range of photometric observables covered by the sample’. In Sheldon et al. (2012), the nearest neighbour weighting algorithm is used to calculate individual redshift probability distributions  $P(z)$  for galaxies in the SDSS Data Release 8.

In this work, along with the more common Euclidean distance, we define and explore two new neighbourhood metrics: the angular neighbourhood and the directional neighbourhood. Using each of these three metrics, we implement two different nearest neighbours approaches: nearest neighbours (kNN) and neighbourhood fitting (NF). The different combinations of algorithms/neighbourhoods are compared. Among them, Directional Neighbourhood Fitting (DNF) stands out as the best performant, and is thus used as one of the photo- $z$  estimators for DES.

The rest of the paper is organized as follows: in Section 2 we introduce the Nearest Neighbour algorithm in the context of photometric redshift estimation and define two new neighbourhoods to address the problem. In Section 3, the SDSS galaxy samples are introduced along with the metrics involved in the comparison. In Section 4, we describe kNN, the most common nearest neighbours approach, and compare it to the new neighbourhoods we have defined. In Section 5, the DNF method is presented and compared with previous approaches. In Section 6, we extend our analysis of DNF to the VIMOS VLT Deep Survey (VVDS) and PHAT datasets, which although smaller samples they provide interesting higher redshift galaxies.

Finally, the conclusions are presented in Section 7.

## 2 PHOTOMETRIC REDSHIFT AND NEIGHBOURHOOD

kNN is an algorithm commonly used for pattern recognition and regression. kNN allows the user to estimate an unknown feature of a specific sample based on its closeness (in the space of observables) to other training samples for which the feature is known. Common kNN algorithms use the Euclidean distance defined in the space of observables as a measurement of closeness or neighbourhood. In this sec-

tion, we define two new neighbourhoods that may provide advantages over the Euclidean metric in some areas.

In the photometric redshift estimation problem, the magnitudes of the galaxies in the set of filters constitute the space of observables. The so-called photometric sample is the set of galaxies represented by points in this space (i.e. galaxies whose magnitudes have been measured) without measured spectra. On the other hand, the training sample is constituted by the set of galaxies for which both magnitudes and spectra have been measured. In order to determine the redshift of a galaxy in the photometric sample, the kNN algorithm uses the training sample as a reference. The photo- $z$  of the target galaxy is obtained from the redshift of training galaxies that are nearby in this multi-magnitude space. The definition of the neighbourhood, the number of near training galaxies considered, and how their redshifts are combined to compute the final photo- $z$  are key elements in ensuring the accuracy of the estimation. The rest of this section focuses on the first of these elements, the neighbourhood.

The redshifts of the training sample form a hypersurface defined over the multi-magnitude space. Given a point in this space, i.e. the galaxy whose redshift is unknown, the surrounding redshift hypersurface may be abrupt or smooth depending on the direction selected. The best local hypersurface fitting will be achieved when the neighbourhood is distributed along a smooth path on the hypersurface. Since the Euclidean neighbourhood treats all directions equally, it may not be the optimal neighbourhood for fitting in many cases. In this section, we explore other neighbourhoods that provide smoother paths.

To illustrate the definitions of the different neighbourhoods and for representativeness we consider a toy example of the space of observables limited to two dimensions. Fig. 1 shows the map of distances corresponding to a point of coordinates (20, 20) in a space of arbitrary observables. Euclidean is the common distance applied in kNN algorithms. Angular and directional are the new neighbourhoods described below that consider galaxies as neighbours taken into account the relative content of the observables, in addition to the absolute one.

### 2.1 Euclidean Neighbourhood

The Euclidean neighbourhood (Fig. 1) defined in the space of observables is the common distance metric used in kNN. The basic idea behind kNN is that closeness among objects in the space of observables implies closeness in terms of other non-observable features. In photometric redshift prediction, the observables are magnitudes or photon fluxes from galaxies. kNN computes the photo- $z$ s of a photometric sample taking a neighbouring spectroscopic training sample as a reference. Thus, the redshift of a galaxy in the photometric sample is computed from the redshifts of its  $k$  nearest neighbours in the training sample. In the following sections, we will use **e-kNN** to refer to Euclidean nearest neighbours. The Euclidean neighbourhood, i.e., the distance between any pair of galaxies in the space of observables, can be quantified by equation 1.

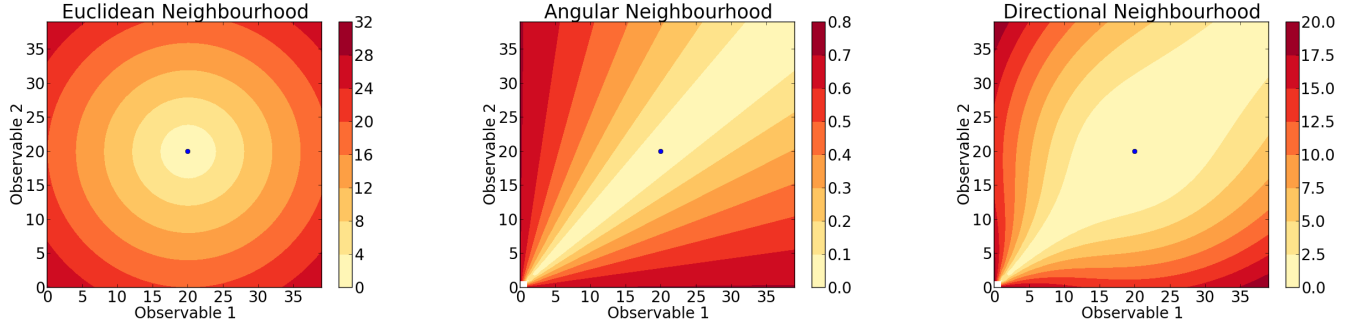


**Figure 1.** Neighbourhoods in two-dimensional space: Euclidean, angular and directional. The colour coding represents the distance to the point (20,20) in the space of observables. Unlike the Euclidean neighbourhood, angular and directional neighbourhoods account for the relative content of observables.

$$D = \sqrt{\sum_{i=1}^n (m_i^t - m_i^p)^2} \quad (1)$$

where  $m^t$  and  $m^p$  are the multi-magnitude vectors of training and photometric galaxies respectively, and  $n$  is the number of bands.

## 2.2 Angular Neighbourhood

Euclidean distance ensures that closely related galaxies in a multi-magnitude space are assigned a similar redshift. However, the Euclidean distance may be improved in some aspects. Note that the Euclidean metric does not count as neighbours galaxies with the same relative multi-magnitude content (e.g. similar colour), but which are separated in overall magnitude. There may be cases of galaxies of the same type, at the same redshift, that differ in size and hence in apparent magnitude. Thus, in spite of having the same redshift they would not be considered as neighbours.

In this work we have considered other metrics to mitigate this drawback of Euclidean neighbourhoods. The first metric explored is the angular Neighbourhood (**a-kNN**; Fig. 1), which is based on the normalized inner product (NIP; equation 2). NIP (Sanchez et al. (2014)) corresponds to the cosine of the angle  $\alpha$  formed by two multi-magnitude vectors. The NIP metric considers two galaxies as neighbours, hence having a close redshift, when they have similar relative multi-magnitude content (e.g. similar colour) rather than absolute multi-magnitude closeness. The metric is based on the inner product definition

$$NIP \equiv \cos \alpha = \frac{\sum_{i=1}^n m_i^t \cdot m_i^p}{\sqrt{\sum_{i=1}^n (m_i^t)^2 \cdot \sum_{i=1}^n (m_i^p)^2}} \quad (2)$$

Higher closeness corresponds to multi-magnitude vectors in the same direction ( $\alpha = 0$ ). In this case proportions among observables of two different objects are maintained, and hence they are neighbours. As shown below, a-kNN improves e-kNN in terms of photo-z dispersion.

## 2.3 Directional neighbourhood

In spite of the lower scatter of a-kNN compared to e-kNN for a few neighbours, the performance of the angular neigh-

**Table 1.** Galaxy selection SQL query

```
SELECT top number of objects
  modelMag_u, modelMag_g, modelMag_r, modelMag_i,
  modelMag_z, modelMagErr_u, modelMagErr_g,
  modelMagErr_r, modelMagErr_i, modelMagErr_z,
  z, objid
FROM SpecPhoto WHERE z between 0.1 and 0.7
```

bourhood degrades quickly when larger neighbourhoods are considered, since it extends in a divergent manner from the target point. To include the benefits of both approaches we have defined the directional neighbourhood (DN; Fig. 1) as the product of Euclidean and angular neighbourhoods:

$$DN = D^2 \sin^2 \alpha \quad (3)$$

where  $D$  is the Euclidean distance (equation 1) and  $\alpha$  is the angle between the two multi-magnitude vectors defined by equation 2.

As shown below (Section 5), the benefits of directional neighbourhood appear not just in terms of the nearest neighbour (**d-kNN**) but in neighbourhood fitting, such that larger neighbourhoods can be considered. In some sense, the Directional metric also accounts for kinship since the relative content of observables (i.e., proportionality) is maintained.

## 3 GALAXY TESTBENCH AND METRICS

### 3.1 Galaxy training and photometric samples

To compare the performance of nearest neighbour photo-zs using different neighbourhood metrics, we selected galaxies from SDSS Data Release 10 (Ahn et al. (2014)). A million objects with known photometry in the SDSS standard *ugriz* filters and with known spectroscopic redshift were selected. The redshift range was  $0.1 < z < 0.7$ . The basic SQL query used for object selection is shown in Table 1.

After excluding a few dozen objects tagged with erroneous magnitudes (*magerr*=9999), the sample was shuffled and divided into two subsamples: 5,000 galaxies as the training sample and the rest as the photometric sample. Note that 5,000 galaxies is enough for training according to our prior tests since it is representative of the photometric sample.

Fig. 2 shows the distribution in redshift and magnitudes of the training and photometric samples. Note that the training sample in this case is a faithful representation

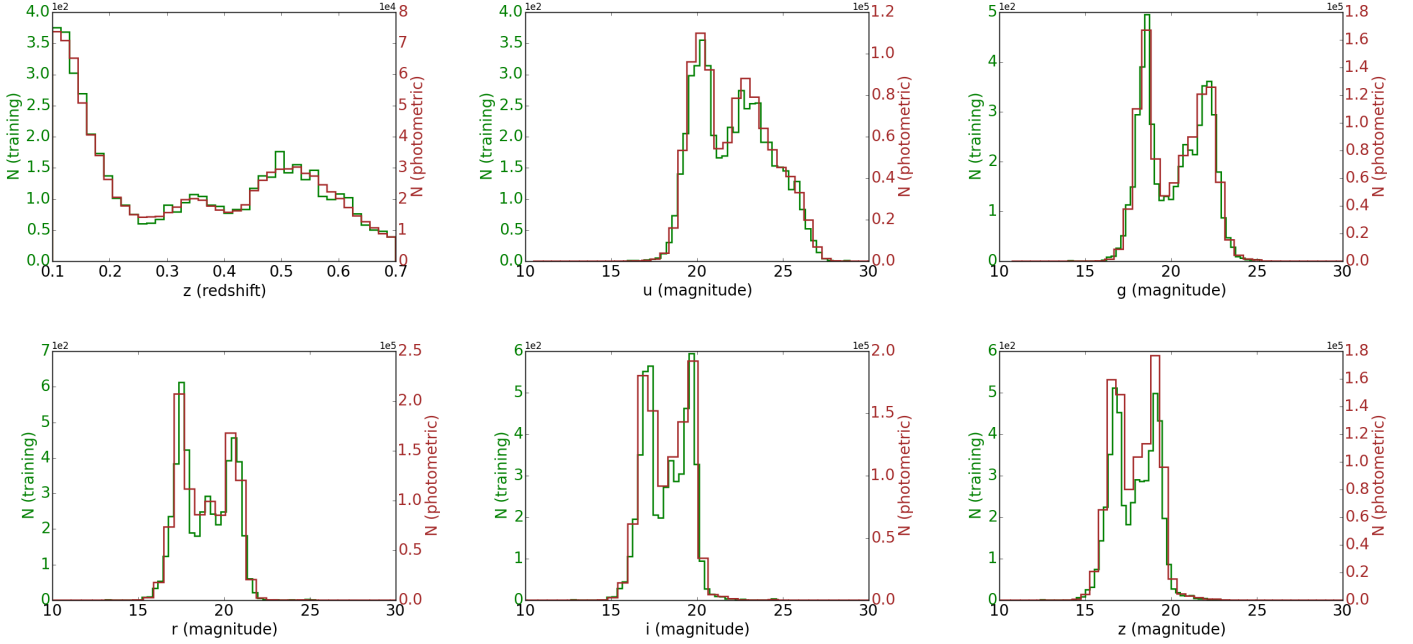


**Figure 2.** True redshift and magnitude distributions of the training and photometric samples of the SDSS dataset used in this work. Note that in each plot the distributions are fully representative of one another.

of the photometric sample both in magnitude and in redshift.

### 3.2 Photometric accuracy and precision metrics

The galaxies of the photometric sample have a set of observables (the magnitudes measured from the five standard SDSS filters *ugriz*) along with the spectroscopic redshift. Since the spectroscopic redshift is known in this case, we can evaluate the accuracy and precision of the photometric redshift estimation. Let  $z_{\text{spec}}$  and  $z_{\text{phot}}$  be the spectroscopic and photometric redshifts, respectively,  $\Delta z = z_{\text{phot}} - z_{\text{spec}}$  be the individual bias and  $N$  be the number of photometric galaxies. Then, the metrics selected to evaluate the photometric redshift estimation are as follows (Sanchez et al. (2014)).

(i) Bias

$$\mu = \frac{1}{N} \sum_{i=1}^N (\Delta z_i) \quad (4)$$

(ii) Dispersion

$$\sigma = \sqrt{\frac{1}{N} \sum_{i=1}^N (\Delta z_i - \text{bias})^2} \quad (5)$$

(iii) Precision in 68-quantile: half the width of the distribution, measured with respect to the median, in which 68% of the data points are enclosed. This is computed as

$$\sigma_{68} = \frac{1}{2} (P_{84} - P_{16}) \quad (6)$$

where

$P_{16}$ =16th percentile of the cumulative distribution

$P_{84}$ =84th percentile of the cumulative distribution

(iv)  $f_{2\sigma}$ : fraction of outliers above the  $2\sigma$  level

$$f_{2\sigma} = \frac{1}{N} \sum_{i=1}^N W_i \quad (7)$$

where

$$W_i = \begin{cases} 1 & \text{if } |\Delta z_i - \text{bias}| > 2\sigma \\ 0 & \text{if } |\Delta z_i - \text{bias}| \leq 2\sigma \end{cases} \quad (8)$$

(v)  $f_{3\sigma}$ : fraction of outliers above the  $3\sigma$  level

$$f_{3\sigma} = \frac{1}{N} \sum_{i=1}^N W_i \quad (9)$$

where,

$$W_i = \begin{cases} 1 & \text{if } |\Delta z_i - \text{bias}| > 3\sigma \\ 0 & \text{if } |\Delta z_i - \text{bias}| \leq 3\sigma \end{cases} \quad (10)$$

(vi)  $N_{\text{Poisson}}$ : a metric to quantify how close the distribution of photometric redshifts  $N(z_{\text{phot}})$  is to the distribution of spectroscopic redshifts  $N(z_{\text{spec}})$ .

Let  $N_i(z_{\text{phot}})$  and  $N_i(z_{\text{spec}})$  be the relative number of photometric and spectroscopic galaxies, respectively, with redshifts in the  $i$ th bin. Then for each photometric redshift bin  $i$  of width 0.05, we compute the difference of  $N_i(z_{\text{phot}})$

and  $N_i(z_{\text{spec}})$ , normalized by the Poisson fluctuations on  $N_i(z_{\text{spec}})$ .

$$N_{\text{poisson}} = \sqrt{\frac{1}{nbins} \sum_{i=0}^{nbins} \frac{(N_i(z_{\text{phot}}) - N_i(z_{\text{spec}}))^2}{N_i(z_{\text{spec}})}} \quad (11)$$

(vii) Kolmogorov-Smirnov test (KS): this statistic quantifies whether the two redshift distributions  $N(z_{\text{phot}})$  and  $N(z_{\text{spec}})$  are compatible with having been drawn from the same parent distribution.

$$KS = \max(|F_{\text{phot}}(z) - F_{\text{spec}}(z)|) \quad (12)$$

where  $F_{\text{phot}}(z)$  and  $F_{\text{spec}}(z)$  are the empirical cumulative distributions functions of  $z_{\text{phot}}$  and  $z_{\text{spec}}$ , respectively.

#### 4 NEAREST NEIGHBOUR COMPARISON

In this section, we use the kNN algorithm to compare the three neighbourhoods described in Section 2: Euclidean, angular and directional. The comparison is performed using the photometric galaxy testbench defined above.

For kNN photometric redshift estimation we select the  $k$  nearest neighbours in magnitude space. The photo- $z$  is then computed as the mean of the redshift of these  $k$  nearest neighbours, pondered inversely to the corresponding distance metric of each neighbour:

$$z_{\text{phot}} = \alpha \sum_{i=1}^k \frac{z_i}{d_i}, \quad (13)$$

where  $\alpha$  is the normalization constant given by

$$\alpha = \frac{1}{\sum_{i=1}^k 1/d_i} \quad (14)$$

To determine the optimum number of neighbours ( $k$ ) to average, we studied the different metrics as a function of the number of neighbours for a random subsample of 50,000 galaxies. The kNN graphs in Fig. 3 show that the bias is stable for e-kNN (light dots) and d-kNN (light diamonds), whereas for a-kNN (light triangles) it grows with the number of neighbours. Regarding the dispersion, it is low and stable beyond 20 neighbours for d-kNN, while for e-kNN and a-kNN, minimums of around 15 and 20 neighbours, respectively, are found. From these plots, d-kNN appears to provide the best compromise between accuracy and precision for the kNN approach.

#### 5 DIRECTIONAL NEIGHBOURHOOD FITTING

In this section, we describe DNF, a new strategy that clearly improves the kNN approaches. DNF computes the photo- $z$  hyperplane that best fits the directional neighbourhood of a photometric galaxy in the training sample. This hyperplane serves as a prediction function for the photo- $z$  of the galaxy considered. Note that since the fitting is local, a linear adjustment (hyperplane) should be sufficient to make a fine

prediction. Let  $\mathbf{m}$  be a multi-magnitude vector in the neighbourhood of the photometric galaxy  $G$ . Then, a generic relationship can be established between redshifts ( $z$ ) and magnitudes ( $\mathbf{m}$ ) in the neighbourhood of  $G$  as shown in equation 15:

$$z = \mathbf{a} \cdot \mathbf{m} \quad (15)$$

where  $\mathbf{a}$  is a parameter vector. This can be computed as the best fit between redshifts and magnitudes of the galaxies in the training sample that are neighbours of  $G$ . Once  $\mathbf{a}$  is computed, equation 15 is applied for the photo- $z$  prediction of the galaxy  $G$ . In addition, the residual of the fit can be considered the photo- $z$  estimated error. The NF method is also applied to the Euclidean and angular neighbourhoods for comparison. We have denoted these methods as Euclidean neighbourhood fitting (**ENF**) and angular neighbourhood fitting (**ANF**), respectively. Regarding the number of neighbours ( $k$ ) used in the fit, a compromise must be found between higher statistical power (larger  $k$ ) and locality (smaller  $k$ ). Fig. 3 shows the dependency of  $\mu$  and  $\sigma$  on  $k$  for the different neighbourhood fitting methods. From the figure, it is noteworthy, that the NF approaches admit a large number of neighbours, and that both accuracy and precision are generally better than obtained with kNN. The difference may be due to a non-optimal weighting scheme for kNN based on the inverse of distance ( $1/d$ ). In addition, DNF (dark diamonds) behaves better than ENF (dark dots) for any value of  $k$ . Thus, ENF bias grows faster with  $k$  than it does in DNF. ENF also shows larger scatter ( $\sigma$ ) in the computed photo- $z$ s than DNF.

##### 5.1 Neighbourhood fitting vs. k-nearest neighbour

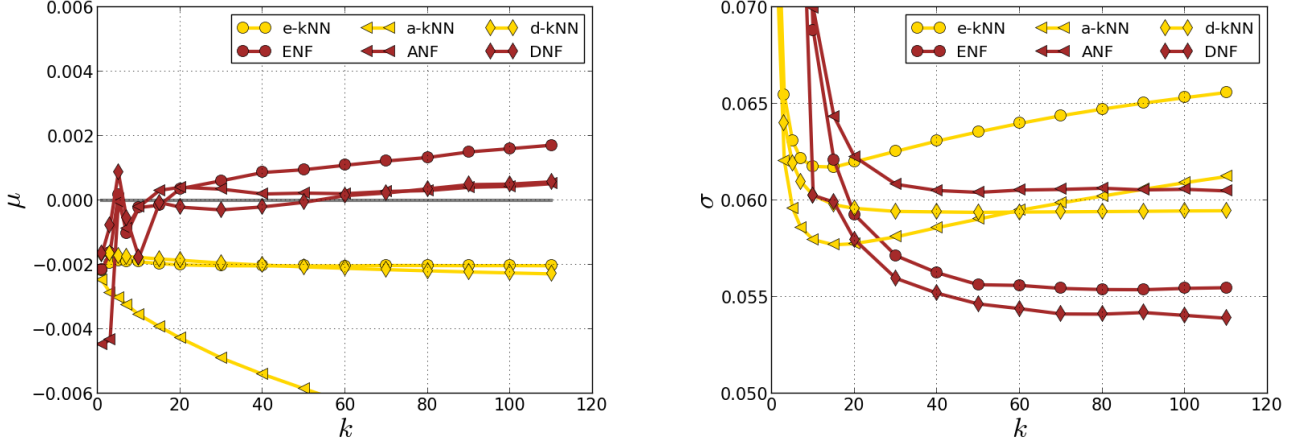
In this subsection, we compare the kNN and NF approaches for the entire photometric sample ( $\sim 1$  million galaxies). The value of  $k$  is fixed at an appropriate value for each method selected in the view of Fig. 3 (25 for kNN and 60 for NF). As a reference, we have also included the results produced by the well-known ANNz algorithm (Collister & Lahav (2004)).

Fig. 4 shows the result of this comparison. Note that  $\mu$ ,  $\sigma$  and  $\sigma_{68}$  perform better for NF than they do for kNN, and at a level close to the reference ANNz. Among the NF approaches, DNF stands out as superior to the other two neighbourhoods for the metrics considered.

Regarding the dependency on the redshift, we focused the study on only three methods: e-kNN (i.e. the common kNN approach), the newly defined DNF method, and the reference ANNz. Fig. 5 shows the comparison in bins of photo- $z$ . DNF behaves better than kNN and similar to ANNz.

In Fig. 6 we can see the scatter plot showing the spectroscopic redshifts ( $z_{\text{spec}}$ ) versus the estimated photometric redshifts ( $z_{\text{phot}}$ ) for the three methods. The DNF approach clearly improves the dispersion seen with kNN and behaves similarly to ANNz for this sample.

With respect to the photo- $z$ s on the edges of the training sample some caveats should be noted. Usually, the redshift limits of the training sample are less populated by galaxies. Finding a fixed number of neighbours in these regions may require moving further away and expanding into regions where the fit is no longer reliable. We have assumed that photo- $z$ s that go beyond the redshift limits of the training



**Figure 3.** Photo- $z$  bias and dispersion metrics as a function of the number of neighbours for Euclidean (dot), angular (triangle) and directional (diamond) neighbourhoods. Light lines correspond to kNN algorithm explained in Section 4 and dark lines to NF described in Section 5.

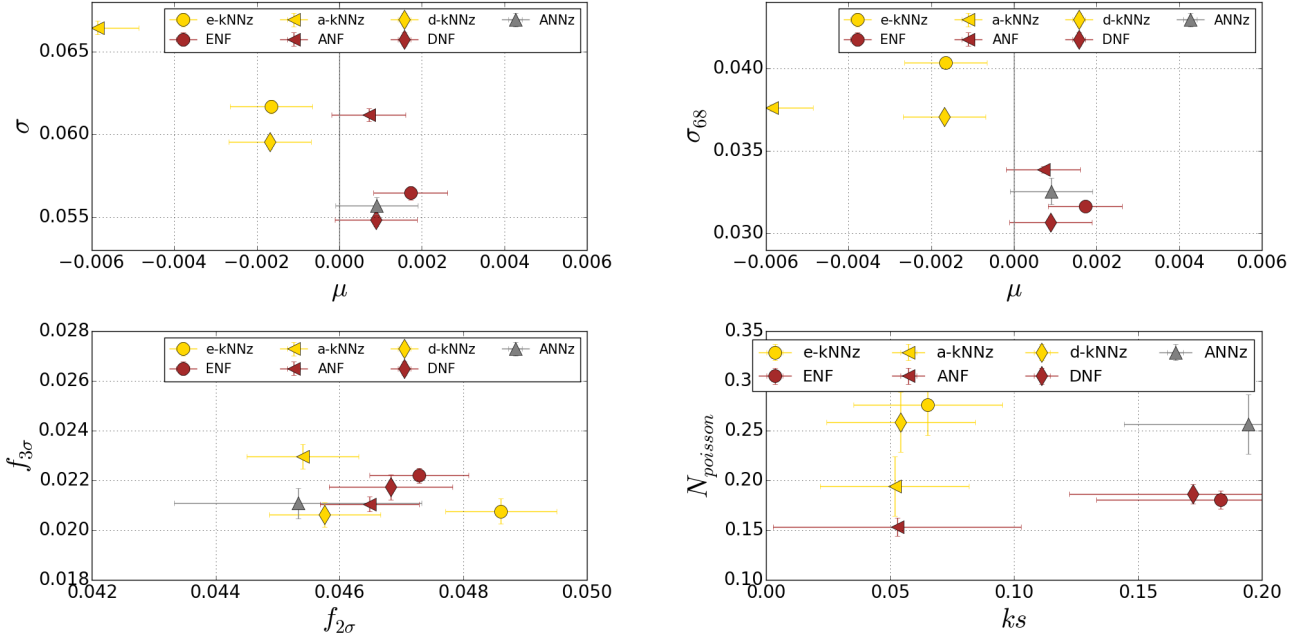


**Figure 4.** Comparison of different combination of nearest neighbour strategies (k-NN and NF) and neighbourhoods (dot: Euclidean; triangle: angular; diamond: directional). Bias versus  $\sigma$ , bias versus  $\sigma_{68}$ ,  $f_{2\sigma}$  versus  $f_{3\sigma}$  outliers, and  $N_{\text{Poisson}}$  versus KS are presented. The plots also show the results produced by the reference code ANNz. DNF produces less bias and scatter than the other codes.

sample are the result of failed non-local fitting. Accordingly, a correction has been applied using the redshift of the nearest neighbour. Another way to circumvent non-local fitting is by limiting the neighbour selection to within a hyper-volume of small radius (or directional radius for directional neighbourhoods). In this approach, the number of neighbours ( $k$ ) depends on the galaxy density of the multi-magnitude space region, and thus, the proper algorithm should be applied. According to Fig. 3, DNF is appropriate for moderate and large values of  $k$  but the fitting process may fail for low values (e.g.  $k < 20$ ). In these cases d-kNN seems to be a safer approach and a hybrid method can be implemented. Finally, it should be noted that a weighting technique, as detailed

in Lima et al. (2008), can also be implemented so that the training sample resembles the photometric sample. This can be done in order to achieve higher representativeness when computing photo- $z$ s.

## 5.2 Photo- $z$ probability density functions

In addition to a single  $z_{\text{phot}}$  value, DNF can produce PDFs which better reflect the uncertainty associated with the photo- $z$  prediction. Let  $s_i$  be the residual of the  $i$ -th neighbour generated in the fit to the hyperplane (equation 16).

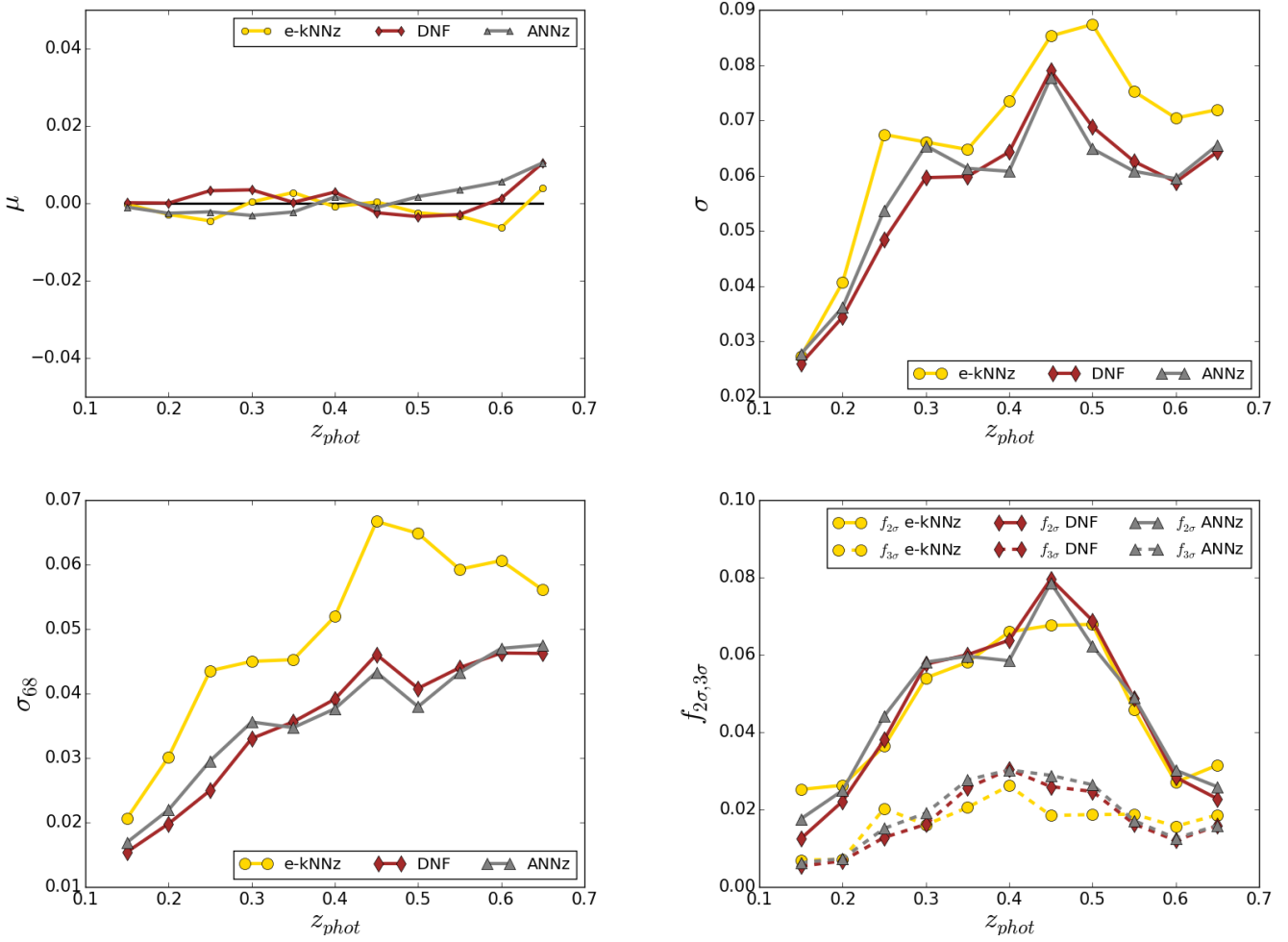


**Figure 5.** Dependence on the redshift of the metrics for the photometric sample for the codes kNN, DNF and ANNz. Note the improvement of DNF with respect to kNN while a similar performance to ANNz is achieved.

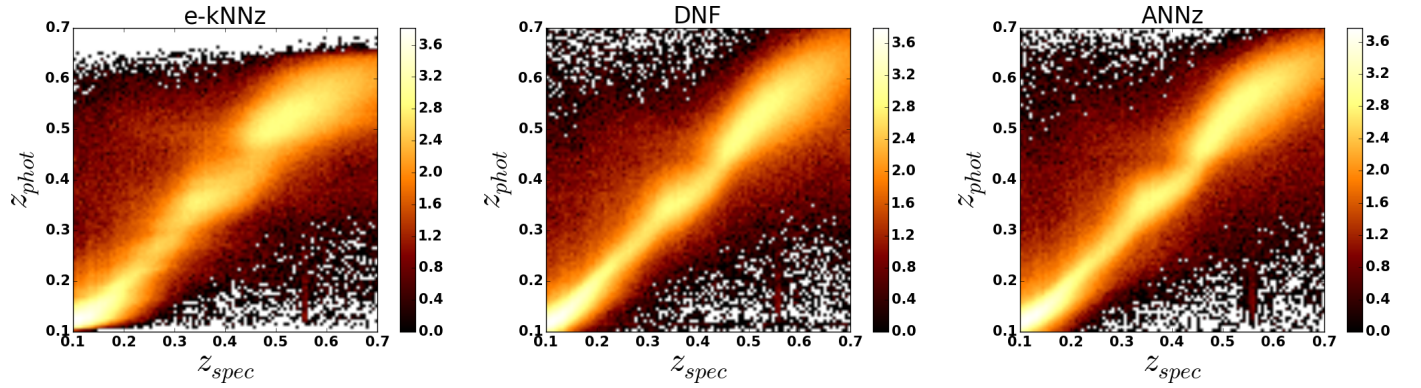


**Figure 6.** Scatter plot ( $z_{\text{photo}}$  versus  $z_{\text{spec}}$ ) for the photometric sample produced by e-kNN (left), DNF (centre) and ANNz (right). Note that DNF clearly improves kNN dispersion and behaves similarly to ANNz.

$$s_i = z_{\text{spec}}^i - a \cdot m_i \quad (16)$$

For each neighbour a PDF sample  $z_i$  is generated by summing the residuals  $s_i$  to  $z_{\text{phot}}$  according to equation 17.

$$z_i = z_{\text{phot}} + s_i \quad (17)$$

The PDF is then obtained by histogramming these samples in redshift bins. Fig. 7 provides some examples of individual photo-z PDFs obtained by Kernel Density Estimation



(KDE) applied to the PDF samples. Note that non-Gaussian uncertainty distributions and degeneracies are reflected by the PDFs computed by DNF.

Fig. 8 shows how the photo- $z$  PDFs also allow us to estimate the uncertainty of the photometric-sample distribution in  $z_{\text{phot}}$  bins. The photometric sample distribution (bars in the graph) in each  $z_{\text{phot}}$  bin is constructed by: (a) classifying the galaxies in bins according to its  $z_{\text{phot}}$ , and (b) histogramming the  $z_{\text{spec}}$  of the galaxies classified in the target  $z_{\text{phot}}$  bin. Estimation of the photometric sample distribution, on the other hand, is done by stacking the photo- $z$  PDFs ( $N(\text{PDFs})$ ) classified in the target bin (dots in the graph).

Fig. 9 shows  $N(z_{\text{spec}})$  (the global photometric-sample distribution) and  $N(\text{PDFs})$ . Note that the shape of the global redshift distribution is well reproduced by stacking the PDFs.

### 5.3 Photo- $z$ error estimation

In addition to photo- $z$  computation, an important issue is the associated error estimation. In kNNz approaches, the standard deviation for the redshift of the  $k$  nearest neighbours in the training sample is considered the photo- $z$  error estimation for the galaxy. In NF methods, as we have already established, the residuals of the fit provide a good estimation of the photo- $z$  bias.

Fig. 10 shows the distribution for the e-kNNz and DNF codes of  $\Delta z / \Delta z_e$  (pull distribution), where  $\Delta z$  is the individual bias and  $\Delta z_e$  is the photo- $z$  error estimation. Note that the ideal pull distribution, which is also drawn, is Gaussian, with  $\mu = 0$  and  $\sigma = 1$ .

Another way to visualize the suitability of the photo- $z$  error estimation is by performing a quality cut based on this parameter. Fig. 11 shows the scatter plot for kNN and DNF, created by selecting the 80% of galaxies per redshift bin that have a smaller photo- $z$  estimated error. Note the good behaviour of DNF, as many of the outliers have been removed.

## 6 APPLICATION OF DNF TO OTHER SURVEY SAMPLES

So far, we have applied DNF to the SDSS DR10 which provides a large number of galaxy spectroscopic redshifts to compare it with. Nevertheless, SDSS DR10 has a very limited redshift range. In this section we extend the comparison to higher redshift. First, we apply DNF to the VVDS sample up to  $z = 1$ . Next, we apply DNF to the public PHAT dataset.

### 6.1 DNF on VVDS

The VVDS is a comprehensive deep galaxy spectroscopic redshift survey conducted by the Visible Imaging Multi-Object Spectrograph (VIMOS) collaboration with the VIMOS multi-slit spectrograph at the ESO-Very Large Telescope (VLT; Garilli et al. (2008)). To evaluate the performance of DNF, we selected 3598 object from the VVDS-F1400+05 dataset. The selected objects are those in the redshift range (0, 1) and with valid magnitude values in the

bands. We split the set into training and validation samples with 2,000 and 1,598 objects respectively. Fig. 12 shows the distribution of redshifts compared to the SDSS sample, and the dependence of the metrics on the redshifts for the codes kNNz, DNF, and ANNz. Note how DNF behaves similarly to ANNz in the central part of the redshift range. The poor behaviour of the codes at the redshift extremes is explained by the shortage of training galaxies. In another view, Fig. 13 provides a summary comparison of the methods. Unlike with kNN, note how DNF achieves accuracy and precision close to ANNz for this set.

### 6.2 DNF on PHAT

The PHAT program is an international initiative whose goal is to test and compare different methods of photo- $z$  estimation. Two different test environments are set up: PHAT0, based on data produced by simulations; and PHAT1, based on data from the Great Observatories Origins Deep Survey (GOODS), including 18-band photometry and 2,000 spectroscopic redshifts. We applied DNF to the PHAT data and evaluated its performance. To provide a fair comparison, we focused only on the training-based methods described in the PHAT paper (note the small size of the training set of 500 objects). The methods used are the following: AN-e (ANNz, artificial neural network), DT-e (BDT, boosted decision trees), EC-e (empirical  $\chi^2$ ), PN-e (nearest neighbour fit), PO-e (polynomial fit), RT-e (regression trees), SN-e (neural network). Table 2 (left) duplicates the PHAT0 comparison (table 3 of the PHAT paper) along with DNF results, where bias and scatter are the mean and the RMS of the quantity  $\Delta z = z_{\text{model}} - z_{\text{phot}}$  (after rejection of outliers) respectively, and the outlier are defined as objects with  $|\Delta z| = |z_{\text{model}} - z_{\text{phot}}| > 0.1$ . Table 2 (right) duplicates the PHAT1 comparison (table 5, columns 5-7 of the PHAT paper) along with DNF results. In this case bias and scatter are the mean and rms of the quantity  $\Delta z' = (z_{\text{spec}} - z_{\text{phot}}) / (1 + z_{\text{spec}})$  respectively and the outliers are defined as objects with  $|\Delta z'| > 0.15$ . Note that DNF are among the best scored training approaches in both the PHAT0 and PHAT1 tests.

## 7 CONCLUSIONS

The precision of many cosmological probes relies on the quality of the photometric redshift technique. Thus, great effort has been put into developing new methods and improving established techniques for both template and training based approaches.

In this paper, we have explored the application of nearest neighbours algorithm to photometric redshift estimation. Two new neighbourhoods (angular and directional) were proposed. The newly defined neighbourhoods, along with the most commonly used, Euclidean neighbourhood, were combined with two nearest neighbour approaches (kNN and NF) to form six methods. In addition the well-known ANNz was used as a reference.

The comparison of methods reveals the value of the new metrics we have defined, especially the DN, which accounts for the relative content of the observables in addition to the absolute one. The results presented for the SDSS dataset



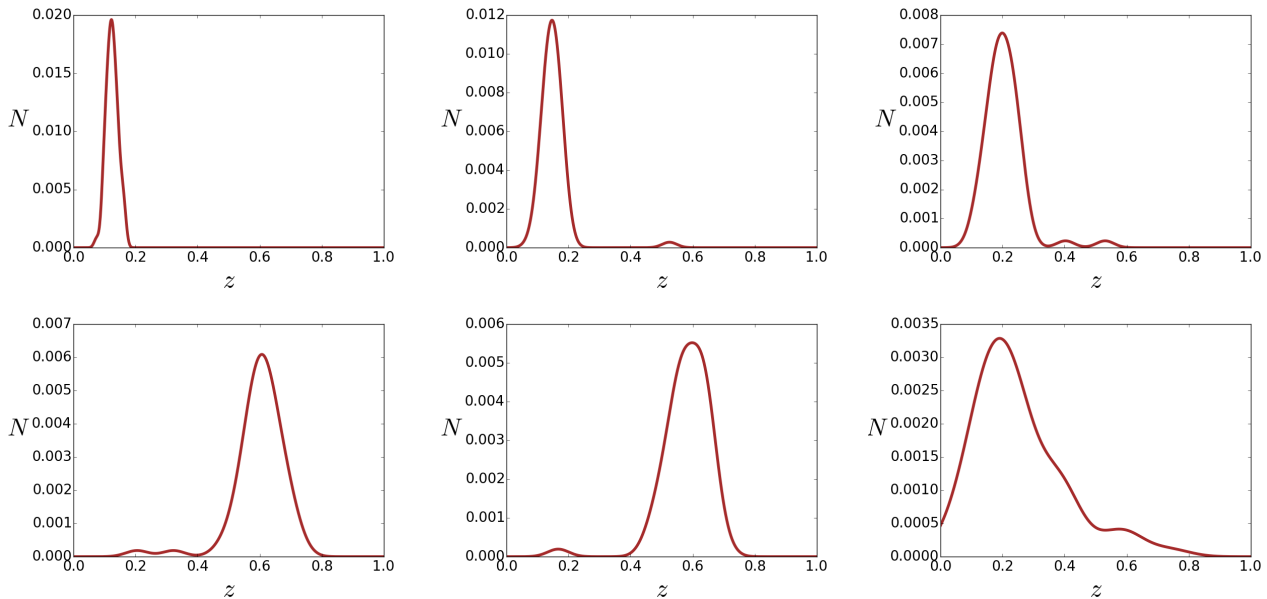


**Figure 7.** Examples of individual photo- $z$  PDF generated by DNF code. Note that the PDF enables the algorithm to capture the uncertainty and degeneracies.

**Table 2.** DNF applied to PHAT data: PHAT0 (left) corresponds to a simulation data. PHAT1 (right) corresponds to GOODS field.

PHAT0				PHAT1			
Code	Bias	Scatter	Outlier (%)	Code	Bias	Scatter	Outlier (%)
AN-e	0.000	0.011	0.018	AN-e	-0.006	0.078	38.5
DT-e	-0.004	0.019	0.389	EC-e	-0.002	0.066	16.7
PN-e	0.000	0.017	0.053	PO-e	-0.007	0.051	13.0
PO-e	0.001	0.019	1.669	RT-e	-0.008	0.067	24.2
RT-e	0.000	0.013	0.010	DNF-e	0.004	0.063	21.0
SN-e	-0.005	0.049	18.202				
DNF-e	0.000	0.011	0.026				

show that the novel DNF method provides the best approximation for photometric redshift estimation among the nearest neighbour approaches explored. Furthermore, extending the tests to the higher redshift datasets of VVDS and PHAT confirms that DNF is among the best scored algorithms.

Another quality of DNF is its ability to compute reliable photo- $z$  PDFs which provide a useful tool for detecting degeneracies and estimating the redshift distribution, both in photo- $z$  bins and for the complete sample. Another key advantage of DNF is that the residuals of the fit directly provide a reliable photo- $z$  error estimation. In conclusion, DNF can be applied to current and future surveys to obtain improved cosmological parameters.

## ACKNOWLEDGEMENTS

Funding support for this work was provided by the Spanish Ministry of Economy and Competitiveness (MINECO) through grant FPA2013-47986-C3-2-P and by the Autonomous Community of Madrid through the project SPACETEC-CM (S2013/ICE-2822). Funding for SDSS-III has been provided by the Alfred P. Sloan Foundation, the Participating Institutions, the National Science Foundation,

and the U.S. Department of Energy Office of Science. The SDSS-III web site is [http : //www.sdss3.org/](http://www.sdss3.org/). SDSS-III is managed by the Astrophysical Research Consortium for the Participating Institutions of the SDSS-III Collaboration including the University of Arizona, the Brazilian Participation Group, Brookhaven National Laboratory, Carnegie Mellon University, University of Florida, the French Participation Group, the German Participation Group, Harvard University, the Instituto de Astrofísica de Canarias, the Michigan State/Notre Dame/JINA Participation Group, Johns Hopkins University, Lawrence Berkeley National Laboratory, Max Planck Institute for Astrophysics, Max Planck Institute for Extraterrestrial Physics, New Mexico State University, New York University, Ohio State University, Pennsylvania State University, University of Portsmouth, Princeton University, the Spanish Participation Group, University of Tokyo, University of Utah, Vanderbilt University, University of Virginia, University of Washington, and Yale University. This research uses data from the VIMOS VLT Deep Survey, obtained from the VVDS database operated by Cesam, Laboratoire d'Astrophysique de Marseille, France. Also, we thank Hendrik Hildebrandt for the analysis of our data in the context of PHAT project.

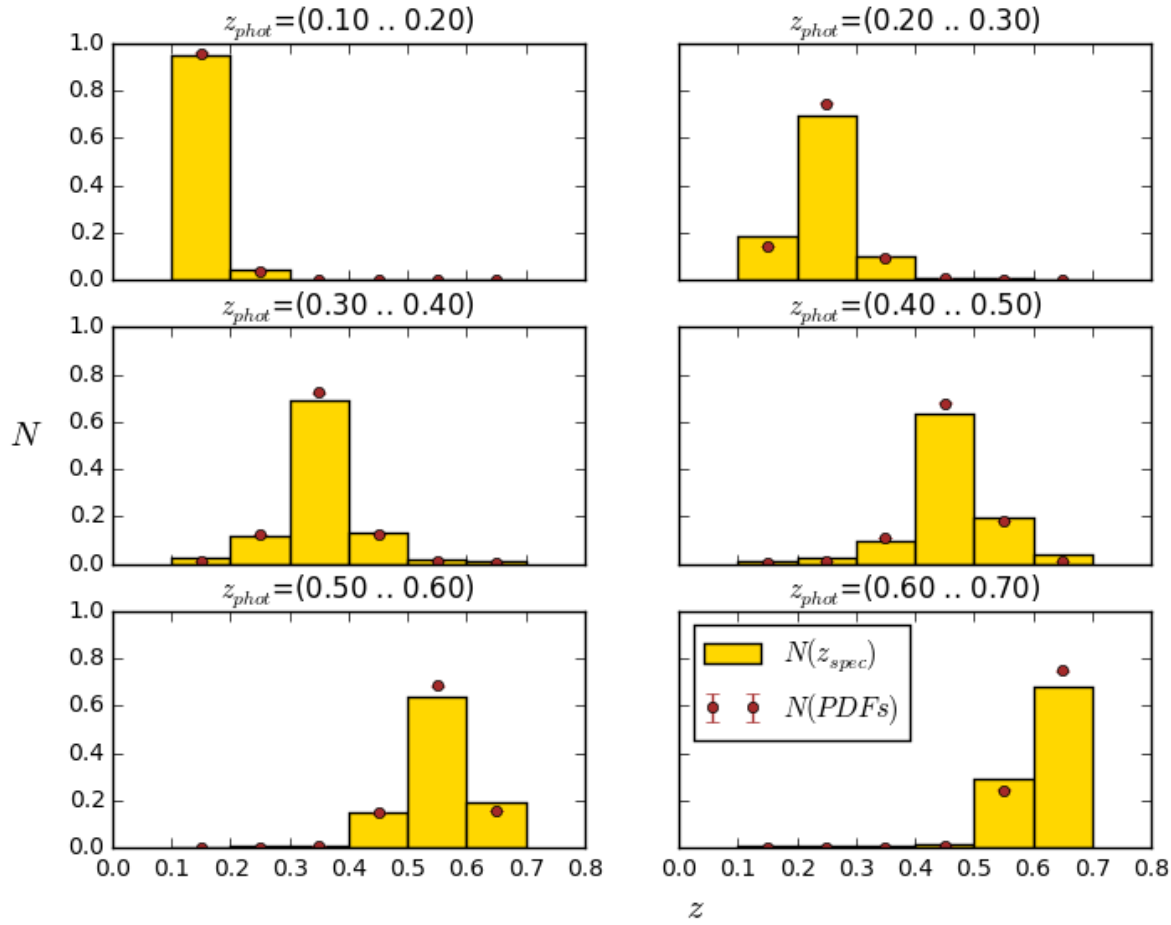


**Figure 8.**  $N(z_{\text{spec}})$  and  $N(\text{PDFs})$  both in  $z_{\text{phot}}$  bins (i.e. galaxies are first classified into bins according to their photo- $z$  and then a comparison between the  $z_{\text{spec}}$  distribution and the PDF stacking is performed for each bin).

## REFERENCES

- Ahn C. P., Alexandroff R., Allende C., et al., 2014, *Astrophysical Journal Supplement Series*, 211
- Altman N. S., 1992, *Journal of the American Statistical Association*, 46, 175
- Arnouts S., Cristiani S., Moscardini L., Matarrese S., Lucchin F., Fontana A., Giallongo E., 1999, *Monthly Notices of the Royal Astronomical Society*, 310, 540
- Ball N. M., Brunner R. J., Myers A. D., 2008, *Astrophysical Journal*, 683, 12
- Benítez N., 2000, *Astrophysical Journal*, 536, 571
- Bolzonella M., Miralles J., Pello R., 2000, *Astronomy and Astrophysics*, 363, 476
- Carrasco M., Brunner R. J., 2013, *Monthly Notices of the Royal Astronomical Society*, 432, 1483
- Collister A. A., Lahav O., 2004, *PASP*, 116, 345
- Connolly A. J., Csabai I., Szalay A. S., Koo D. C., Kron R. G., Munn J. A., 1995, *Astronomical Journal*, 110, 2655
- Csabai I., Budavari T., Connolly A. J., 2003, *The Astronomical Journal*, 125, 580
- Csabai I., Dobos L., Trencseni M., 2007, *Astronomische Nachrichten*, 328, 852
- Feldmann R., et al., 2006, *Monthly Notices of the Royal Astronomical Society*, 372, 565
- Flaugher B., et al., 2005, *Journal of Modern Physics A*, 20, 3121
- Garilli et al., 2008, *Astronomy and Astrophysics*, 486, 683
- Gerdes D., Sypniewski A. J., et al., 2010, *Astrophysical Journal*, 715, 823
- Hildebrandt H., et al., 2010, *Astronomy and Astrophysics*, 523, A31
- Hoyle B., Rau M. M., R. Z., Seitz S., Weller J., 2015, *Monthly Notices of the Royal Astronomical Society*, 449, 1275
- Ivezić Ž., et al., 2013, *LSST Science Requirements Document*
- Lima M., Cunha C. E., Oyaizu H., Frieman J., Lin H., Sheldon E. S., 2008, *Monthly Notices of the Royal Astronomical Society*, 390, 118
- Oyaizu H., Lima M., Cunha C. E., Lin H., Frieman J., Sheldon E. S., 2008, *Astrophysical Journal*, 674, 768
- Rau M. M., Seitz S., Brimiouille F., Frank E., Friedrich O., Gruen D., 2015, *Monthly Notices of the Royal Astronomical Society*, 452, 3710
- Sanchez C., Carrasco M., Lin H., et al., 2014, *Monthly Notices of the Royal Astronomical Society*, 445, 1482

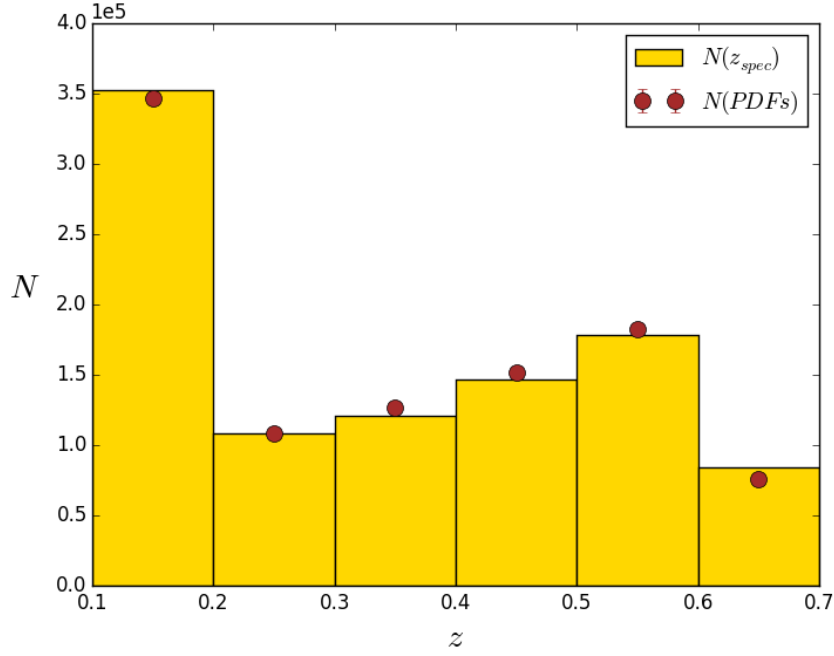


**Figure 9.**  $N(z_{\text{spec}})$  versus  $N(\text{PDFs})$  for the photometric sample. Note that the measured distribution is well estimated by stacking photo-z PDFs.

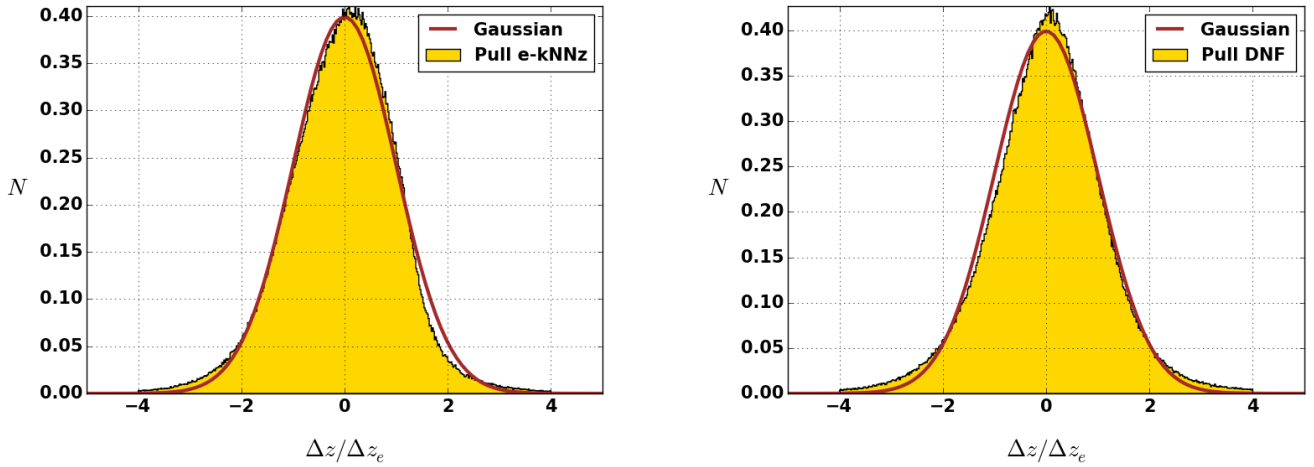


**Figure 10.** Pull:  $\Delta z/\Delta z_e$  distribution for e-kNN (left) and DNF (right). Also drawn is the ideal pull distribution, which is a Gaussian, with  $\mu = 0$  and  $\sigma = 1$ .

Sheldon E. S., Cunha C. E., Mandelbaum R., Brinkmann J., Weaver B. A., 2012, *Astrophysical Journal Supplemental Series*, 201, 32

Wang D., Zhang Y., Zhao Y., 2010, *Proc. SPIE*, 7740, 77402O

Zhang Y., Ma H., Peng N., Zhao Y., Wu X., 2013, *The Astronomical Journal*, 146, 22

Zheng H., Zhang Y., 2012, in *Society of Photo-Optical Instrumentation Engineers (SPIE) Conference Series Vol. 8451 of Society of Photo-Optical Instrumentation Engineers (SPIE) Conference Series*, Review of techniques for photometric redshift estimation

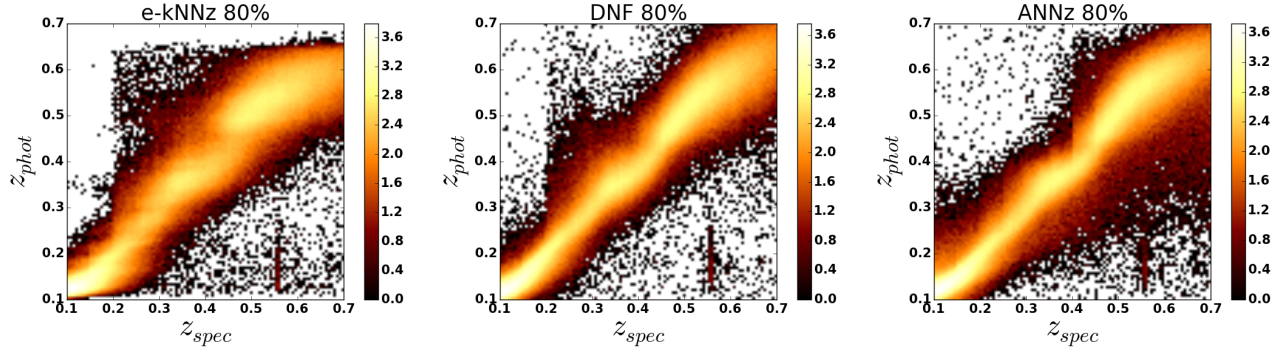


**Figure 11.** Scatter plot ( $z_{\text{photo}}$  versus  $z_{\text{spec}}$ ) for the photometric sample with a quality cut of the 80% of the galaxies with the best photo- $z$  error estimation, applied in bins of  $\Delta z = 0.05$ , and provided by the codes e-kNN (left), DNF (centre) and ANNz (right).

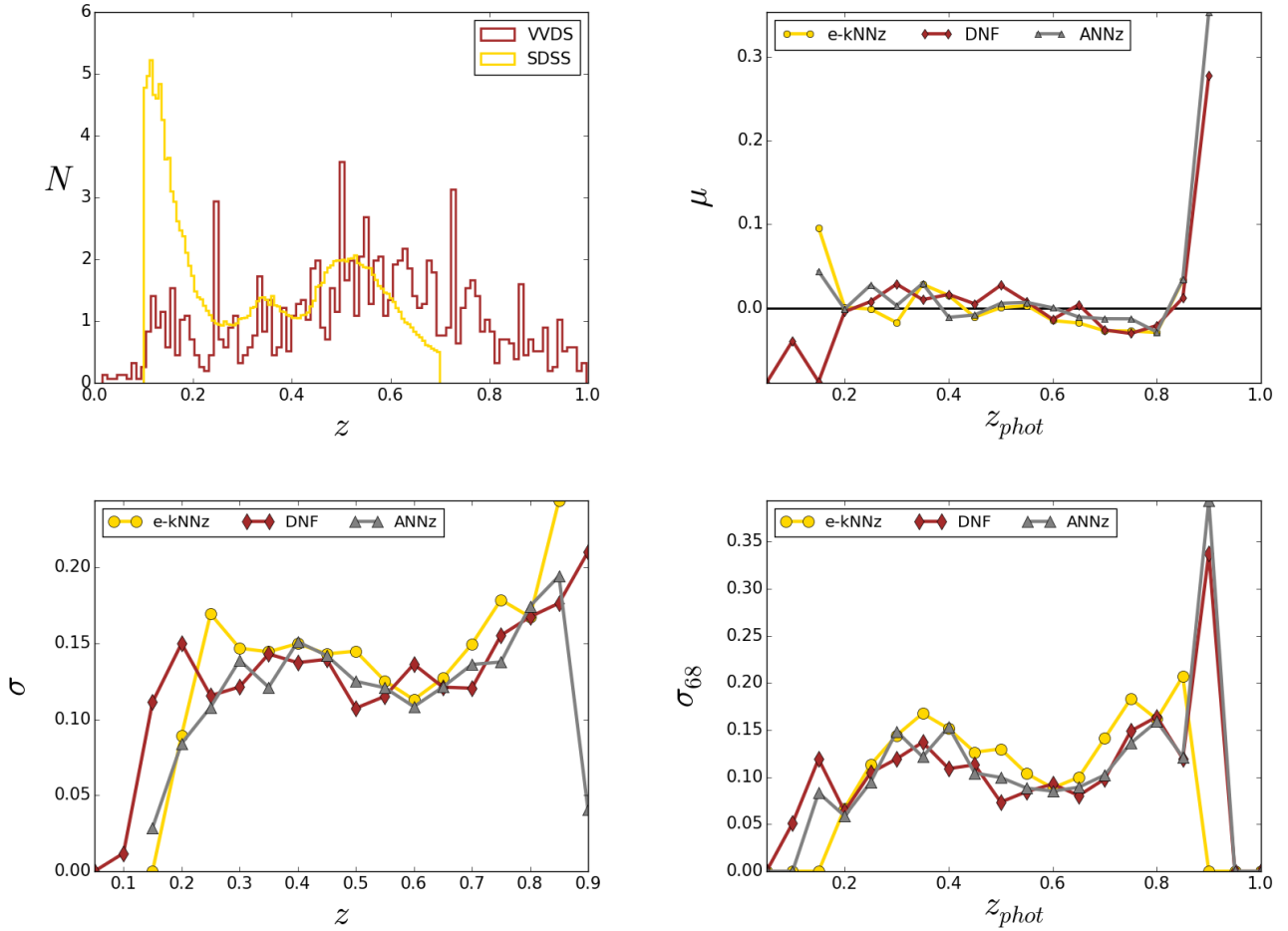


**Figure 12.** VVDS redshift distribution  $N(z_{\text{spec}})$  of the photometric sample compared to the SDSS sample (upper left). The rest of the figures show the dependence of the metrics on  $z$  for the codes kNN, DNF and ANNz. Note how DNF behaves similar to ANNz in the central part of the redshift range. The strange behaviour of the plots at the redshift extremes is explained by the shortage of training galaxies.

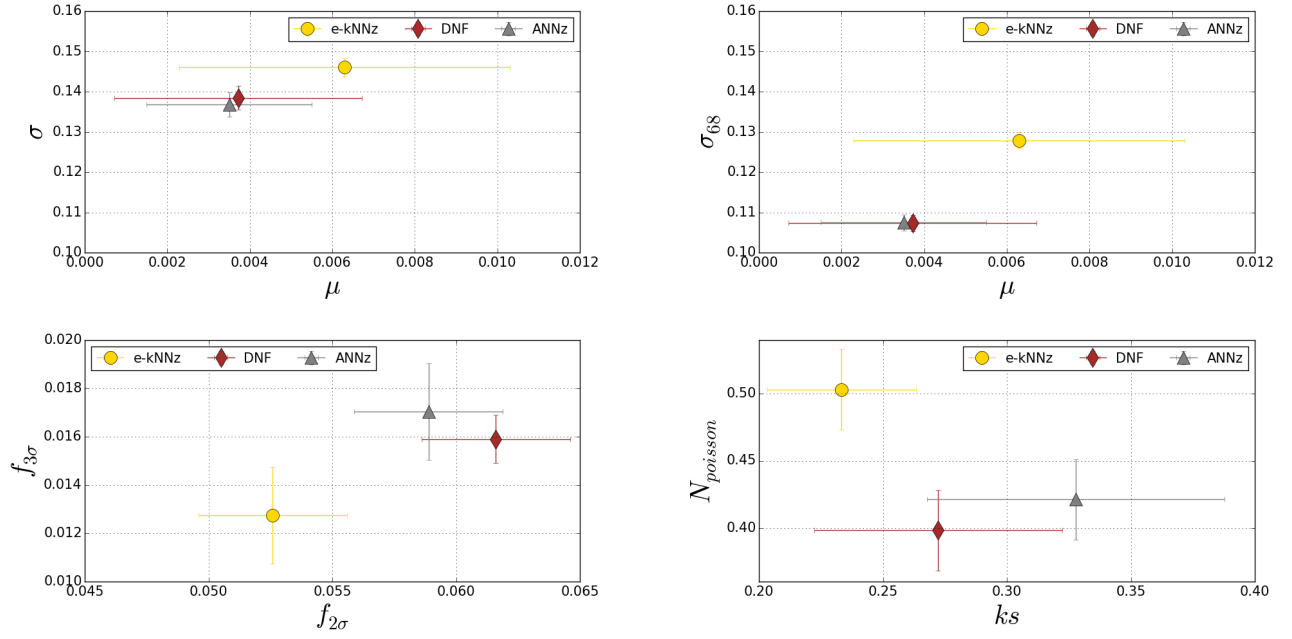


**Figure 13.** Comparison among kNN, DNF and ANNz for the VVDS sample up to  $z = 1$ . Bias versus  $\sigma$ , bias versus  $\sigma_{68}$ ,  $f_{2\sigma}$  versus  $f_{3\sigma}$  outliers and  $N_{\text{Poisson}}$  versus KS are represented.